2013 IEEE/RSJ International Conference on
Intelligent Robots and Systems (IROS)
November 3-7, 2013. Tokyo, Japan

Nonlinear Control of VTOL UAVs Incorporating Flapping Dynamics

Sammy Omari, Minh-Duc Hua, Guillaume Ducard, *Member, IEEE,* Tarek Hamel, *Member, IEEE*

***Abstract*— This paper presents the design and evaluation of a nonlinear control scheme for multirotor helicopters that takes first-order drag effects into account explicitly. A dynamic model including the blade flapping and induced drag forces is presented. Based on this model, a hierarchical nonlinear controller is designed to actively compensates for the nonlinear effects these drag forces. Reported simulation and experimental results indicate the significant performance improvement of the proposed drag-augmented control scheme with respect to a conventional nonlinear controller. For completeness, an offline procedure allowing for efficiently identifying the drag parameters is proposed.**

I. Introduction

In early works on modeling of small-scale multirotor helicopters [6], the interaction between the propellers and the vehicle's dynamics was often neglected, in particular the blade flapping and induced drag dynamics. In fact, these aerodynamic phenomena have been thoroughly studied in the literature for classical, large-scale helicopters (e.g. [14]). Only recently have these aerodynamic drag forces been taken into account for the modeling of small-scale quadrotors [13], [10], [1], [9]. So far, the flapping dynamics of multirotor UAVs have been used mainly for estimation purposes, i.e. to improve the estimation of the translational velocity of a multirotor system [1] or for a better understanding the role of accelerometer measurement in feedback control [10].

Even though these drag forces are significant, they have been mostly neglected in the design of a control scheme. This might be due to the fact that these forces are of a dissipative nature and contribute to the stability of the vehicle during hovering. However, during trajectory tracking these forces become a disturbance and should be accounted for in the control design for an improved flight performance.

In [13], [10] and [1], some linear controllers are proposed that are taking into account the first order drag forces. The UAV model is linearized at hovering and the controllers are derived using classical linear control methods.

Inspired by those works, a drag-augmented nonlinear control approach is developed for a high tracking performance, while ensuring a large domain of stability. The particularity and difficulty of the control design are typically related to the fact that the first-order drag forces depend on the UAVs orientation that may result in the non-existence of a closed form control solution. The solution proposed in the present paper concerns an appropriate change of variables that allows one to approximately rewrite the system dynamic equation, in which the new external force vector is no longer a function of the UAVs orientation.

We show that, during trajectory tracking, these drag forces are a significant disturbance to classical controllers and are typically counteracted using an integral control term. Since this disturbance is not slowly time-varying, this integral action can result in unsatisfying control performance. The drag-augmented controller takes into account these forces, thus reducing the need for integral control action, which results in an improved control performance.

Due to its cascaded structure, the proposed control scheme is simple to implement and tune, with a real-time computational effort comparable to the one required with linear controllers. It can be viewed as a natural extension of linear controllers and, therefore, be tuned using linear control gain optimization techniques.

II. System Modeling

This section presents the mathematical flight model used throughout this work. The most basic multirotor helicopter configuration consists of a rigid airframe with two pairs of counter-rotating rigid propellers attached to it. Control of this platform is achieved by varying the rotational speed of the rotors. While such a four-rotor configuration already allows for full actuation of the vehicle's attitude, this configuration can be scaled up to an arbitrary number of rotors, however, the configuration should always consist of a multiple of counter-rotating rotor pairs for torque balancing reasons. In Fig. 1, a schematic of the Flybox hexacopter, used for the experimental validation of the proposed control scheme, is depicted.

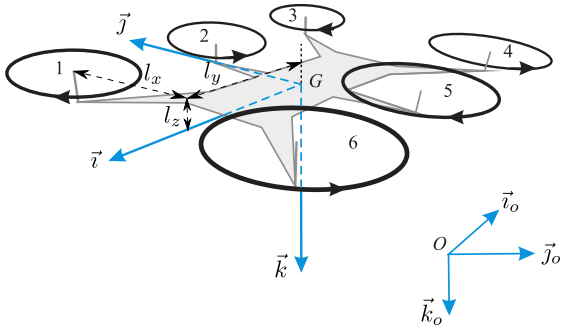

Fig. 1. Schematic representation of a six-rotor UAV platform. Inertial frame with origin O is denoted $\mathcal{I}$ and the body-fixed frame with origin G is denoted $\mathcal{B}$.

First, the following notation is introduced (see Fig. 1). The vehicle's center of mass (CoM) is denoted as G, its mass m,

Sammy Omari is with the Autonomous Systems Lab, ETH Zurich, Switzerland and Skybotix AG. E-mail: $omaris@ethz.ch$.
Minh-Duc Hua is with ISIR CNRS-UPMC, France. E-mail: $hua@isir.upmc.fr$.
Guillaume Ducard and Tarek Hamel are with I3S UNS-CNRS, France. E-mail: $ducard(thamel)@i3s.unice.fr$.

and its inertia matrix $\mathbf{J}$. Let $\mathcal{I} = \{O; \vec{\imath}_o, \vec{\jmath}_o, \vec{k}_o\}$ and $\mathcal{B} = \{G; \vec{\imath}, \vec{\jmath}, \vec{k}\}$ denote the inertial frame (i.e. world frame) and the frame attached to the vehicle (i.e. body-fixed frame), respectively. Let $\boldsymbol{\xi} \in \mathbb{R}^3$ denote the position of the vehicle's CoM expressed in $\mathcal{I}$. The rotation matrix representing the orientation of the frame $\mathcal{B}$ relatively to the frame $\mathcal{I}$ is $\mathbf{R} \in SO(3)$. The vehicle's velocity and the wind velocity are both expressed in the frame $\mathcal{I}$ are denoted as $\dot{\boldsymbol{\xi}} \in \mathbb{R}^3$ and $\dot{\boldsymbol{\xi}}_w \in \mathbb{R}^3$, respectively. The vehicle's velocity in the body-fixed frame is $\mathbf{v} = \mathbf{R}^\top \dot{\boldsymbol{\xi}}$. Let $\boldsymbol{\omega} \in \mathbb{R}^3$ be the angular velocity of the frame $\mathcal{B}$ expressed in $\mathcal{B}$. Let $\varpi_i \in \mathbb{R}$ denote the angular velocity of the rotor of index i. The radius of the propeller is denoted as r. The canonical basis of $\mathbb{R}^3$ is denoted $\{\mathbf{e}_1, \mathbf{e}_2, \mathbf{e}_3\}$. Let $\mathbf{d}_i = [d_{1,i}\, d_{2,i}\, d_{3,i}]^\top \in \mathbb{R}^3$ be the displacement of the i-th rotor from the vehicles CoM expressed in the body-fixed frame $\mathcal{B}$. We define $\mathbf{d}_i^\perp = [d_{1,i}\, d_{2,i}\, 0]^\top \in \mathbb{R}^3$ as the component of $\mathbf{d}_i$ perpendicular to $\mathbf{e}_3$. The notation $_\times$ represents the skew-symmetric matrix associated with the cross product, i.e. $\mathbf{u}_\times \mathbf{v} = \mathbf{u} \times \mathbf{v}$, $\forall \mathbf{u}, \mathbf{v} \in \mathbb{R}^3$. The Euclidean norm in $\mathbb{R}^n$ is denoted as $|\cdot|$.

A. Dynamic Model of Vehicle

Following the model proposed in [6], the i-th rotor, turning at ϖ_i, generates a thrust force $\mathbf{F}_{t,i} = T_i \mathbf{e}_3$, with $T_i = c_T \varpi_i^2$, and an aerodynamic torque $\mathbf{Q}_i = \lambda_i c_Q \varpi_i^2 \mathbf{e}_3$ with the aerodynamic constants c_T, c_Q and $\lambda_i = \{-1, 1\}$, depending on the direction of rotation of the rotor (cw: $\lambda_i = 1$, ccw: $\lambda_i = -1$). Additionally, each rotor imposes a drag force $\mathbf{F}_{d,i}$ on the vehicle due to blade flapping and induced drag, as explained in more detail in Sec. II-B. The remaining aerodynamic forces and torques (mostly due to form drag caused by the fuselage) are summed up in a vector $\mathbf{F}_{aero} \in \mathbb{R}^3$ and $\boldsymbol{\Gamma}_{aero} \in \mathbb{R}^3$ respectively. The vehicle is subject to gravity $mg\mathbf{e}_3$.

Applying the Newton-Euler formalism, one obtains the following equations of motion of the vehicle [8]:

$$\begin{cases} m\ddot{\boldsymbol{\xi}} &= \mathbf{R}\sum_i \mathbf{F}_i + mg\mathbf{e}_3 + \mathbf{F}_{aero} & \text{(1a)} \\ \dot{\mathbf{R}} &= \mathbf{R}\boldsymbol{\omega}_\times & \text{(1b)} \\ \mathbf{J}\dot{\boldsymbol{\omega}} &= -\boldsymbol{\omega}_\times \mathbf{J}\boldsymbol{\omega} + \sum_i (\mathbf{Q}_i + \mathbf{d}_i \times \mathbf{F}_i) + \boldsymbol{\Gamma}_{aero} & \text{(1c)} \end{cases}$$

with $\mathbf{F}_i$ the sum of thrust and drag force generated by each rotor, i.e. $\mathbf{F}_i = \mathbf{F}_{t,i} + \mathbf{F}_{d,i}$.

B. Rotor Aerodynamics

Blade flapping and induced drag are of significant importance for understanding the natural stability of multirotor systems. These forces require special attention since they act on the rotor plane and thus affect the underactuated translational dynamics of the UAV. Aerodynamic drag due to blade flapping affects the UAV in forward flight. More precisely, when the UAV is in forward flight, the advancing rotor blade has a higher tip velocity and will therefore generate more lift than the retreating blade. Since the rotor blades are not completely rigid, the advancing blade rises due to the increased lift as it advances into the direction of flight and the retreating blade as it moves in the opposite direction. This up-down movement (flapping) of the blade remains in an equilibrium in a constant speed forward flight. In this equilibrium, the rotor will have a constant tilt-angle away from the forward velocity of the UAV. Since the thrust of the rotor is perpendicular to the tilted rotor plane, the horizontal component of the thrust can be seen as a damping force counteracting the current forward velocity, as depicted in Fig. 2. For any kind of airfoil generating lift, there is

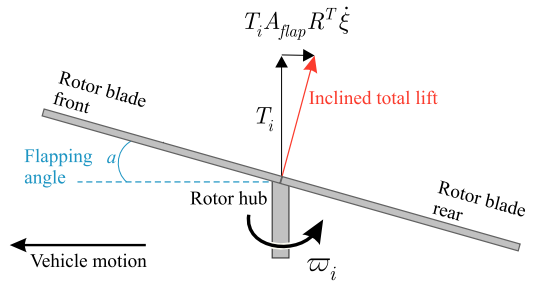

Fig. 2. Aerodynamic drag due to blade flapping. Difference in relative wind speed in forward flight for the advancing and retreating rotor blade causes the rotor plane to tilt, thus causing a force pointing in the opposite direction. Schematic inspired by [9].

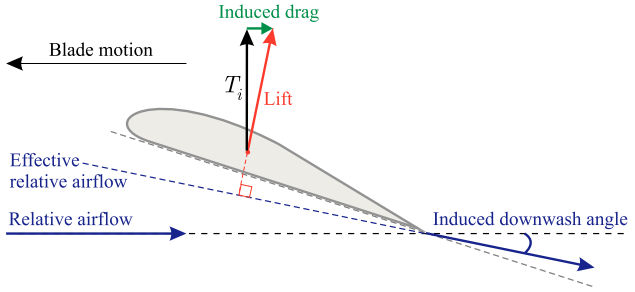

Fig. 3. Aerodynamic force due to induced drag.

an associated induced drag proportional to the lift that it produces, as depicted in Fig. 3. This is due to the fact, that the lift generated by the airfoil is tilted backwards by an angle corresponding to the induced downwash angle. During hovering, the forces are equally distributed and are responsible for the aerodynamic torque $\mathbf{Q}_i$. However, in forward flight, the advancing blade experiences more lift and therefore generates more induced drag as the retreating one. This results in a net force that is opposing the current forward velocity.

Rotor blades on small-scale multirotor helicopters are usually hingeless, i.e. they have no articulated rotor head. However, since they are usually not rigid, the aerodynamic and inertial forces on the rotors during flight can cause the rotors to bend.

We can write the blade flapping dynamics as instantaneous functions of the vehicles velocity since the blade flapping dynamics are very fast compared to the vehicle dynamics. To model the effect of blade flapping on the vehicle, we first compute the advance ratio μ_{ri} and azimuthal direction ψ_{ri} of each rotor

$$\mathbf{v}_{ri} = \mathbf{R}^\top (\dot{\boldsymbol{\xi}} - \dot{\boldsymbol{\xi}}_w) + \boldsymbol{\omega} \times \mathbf{d}_i,$$
$$\mu_{ri} = \frac{|\mathbf{v}_{ri,1,2}|}{\varpi_i r}, \quad \psi_{ri} = \arctan 2(v_{ri,2}, v_{ri,1}),$$

where $\mathbf{v}_{ri}$ is the linear velocity that the i-th rotor hub experiences. Proposed by [13], [9], the lateral and longitudinal flapping angles a_i and b_i can be computed as

$$\begin{bmatrix} a_i \\ b_i \end{bmatrix} = \begin{bmatrix} C\psi_{ri} & -S\psi_{ri} \\ S\psi_{ri} & C\psi_{ri} \end{bmatrix} \begin{bmatrix} a_{si} \\ b_{si} \end{bmatrix},$$

$$a_{si} = \frac{c_a \mu_{ri}}{1 - \frac{\mu_{ri}^2}{2}}, \quad b_{si} = \frac{c_b \mu_{ri}}{1 + \frac{\mu_{ri}^2}{2}},$$

with c_a and c_b denoting some positive parameters. One deduces that

$$\begin{bmatrix} a_i \\ b_i \end{bmatrix} = \begin{bmatrix} \frac{c_a}{1-\frac{\mu_{ri}^2}{2}} & -\frac{c_b}{1+\frac{\mu_{ri}^2}{2}} \\ \frac{c_b}{1+\frac{\mu_{ri}^2}{2}} & \frac{c_a}{1-\frac{\mu_{ri}^2}{2}} \end{bmatrix} \mathbf{v}_{ri,1,2} \approx \begin{bmatrix} c_a & -c_b \\ c_b & c_a \end{bmatrix} \mathbf{v}_{ri,1,2},$$

where the last approximation is justified by the fact that the vehicle's velocity is small compared to the propeller tip velocity so that the term $\frac{\mu_{ri}^2}{2}$ can be neglected compared to 1. From here, one verifies that

$$\begin{aligned} \sum_i \mathbf{F}_i &= \sum_i (\mathbf{F}_{t,i} + \mathbf{F}_{d,i}) = -T\mathbf{e}_3 - c_T \mathbf{A}_{flap} \sum_i \varpi_i^2 \mathbf{v}_{ri} \\ &= -T\mathbf{e}_3 - T\mathbf{A}_{flap}(\mathbf{R}^\top(\dot{\boldsymbol{\xi}} - \dot{\boldsymbol{\xi}}_w) - d_{3,i}\boldsymbol{\omega} \times \mathbf{e}_3) \\ &\quad + \mathbf{A}_{flap}\,\boldsymbol{\omega} \times \sum_i T_i \mathbf{d}_i^\perp \end{aligned} \tag{2}$$

with the flapping matrix $\mathbf{A}_{flap} := \begin{bmatrix} c_a & -c_b & 0 \\ c_b & c_a & 0 \\ 0 & 0 & 0 \end{bmatrix}$ and the thrust magnitude

$$T = c_T \sum_i \varpi_i^2, \tag{3}$$

We can further simplify Eq. (2) to

$$\sum_i \mathbf{F}_i = -T\mathbf{e}_3 - T\mathbf{A}_{flap}\mathbf{R}^\top \dot{\boldsymbol{\xi}} \tag{4}$$

by assuming that the wind speed $\dot{\boldsymbol{\xi}}_w$ is negligible, the vertical distance of the rotor plane to the CoM is very small ($d_{3,i}\boldsymbol{\omega} \times \mathbf{e}_3 \approx 0$) and that the yaw angular rates of the vehicle are negligible ($\mathbf{A}_{flap}\,\boldsymbol{\omega} \times \sum_i T_i \mathbf{d}_i^\perp \approx 0$).

The drag force caused by the induced drag in forward flight can be modeled by $\mathbf{F}_{i.d.} = -T\mathbf{A}_{i.d.}\mathbf{R}^\top \dot{\boldsymbol{\xi}}$, with $\mathbf{A}_{i.d.} = \text{diag}(c_{dx}, c_{dy}, 0)$ where c_{dx}, c_{dy} are the induced drag coefficients [9]. Due to the similar nature of the drag terms caused by flapping and induced drag, we can summarize all the drag in a lumped parameter model as

$$\sum_i \mathbf{F}_i = -T\mathbf{e}_3 - T\mathbf{A}_{drag}\mathbf{R}^\top \dot{\boldsymbol{\xi}} \tag{5}$$

with $\mathbf{A}_{drag} = \mathbf{A}_{flap} + \mathbf{A}_{i.d.}$.

Equivalently to the translational dynamics, the effect of the drag forces on the rotational dynamics can be expressed as

$$\sum_i \mathbf{Q}_i + \mathbf{d}_i \times \mathbf{F}_i = \boldsymbol{\Gamma} - \sum_i T_i \mathbf{d}_i \times \mathbf{A}_{drag}\mathbf{v}_{ri} \tag{6}$$

with

$$\boldsymbol{\Gamma} = \sum_i \lambda_i c_Q \varpi_i^2 \mathbf{e}_3 - c_T \varpi_i^2 \mathbf{d}_i^\perp \times \mathbf{e}_3. \tag{7}$$

C. Model for Control Design and Rate Control

The UAV model (1) can be rewritten as

$$\begin{cases} \Sigma_1 : \begin{bmatrix} m\ddot{\boldsymbol{\xi}} \\ \dot{\mathbf{R}} \end{bmatrix} = \begin{bmatrix} -T\mathbf{R}\mathbf{e}_3 + \mathbf{F}_e \\ \mathbf{R}\boldsymbol{\omega}_\times \end{bmatrix} & \text{(8a)} \\ \Sigma_2 : \ \mathbf{J}\dot{\boldsymbol{\omega}} = -\boldsymbol{\omega}_\times \mathbf{J}\boldsymbol{\omega} + \boldsymbol{\Gamma} + \boldsymbol{\Gamma}_e & \text{(8b)} \end{cases}$$

where $\mathbf{F}_e$ and $\boldsymbol{\Gamma}_e$ are the sum of all the acting forces and moments on the vehicle except the thrust force $T\mathbf{R}\mathbf{e}_3$ and the torque $\boldsymbol{\Gamma}$ by the rotors defined by Eqs. (3) and (7) respectively.

From Eqs. (3) and (7), one can view $T \in \mathbb{R}^+$ and $\boldsymbol{\Gamma} \in \mathbb{R}^3$ as control inputs of System (8). For N mounted rotors, we can rewrite Eq. (3) as a linear mapping from the square of the propellers' angular velocity to the total thrust T and torque $\boldsymbol{\Gamma}$:

$$\begin{bmatrix} T \\ \boldsymbol{\Gamma} \end{bmatrix} = \begin{bmatrix} c_T & c_T & \dots & c_T \\ c_T\, d_{2,1} & c_T\, d_{2,2} & \dots & c_T\, d_{2,N} \\ -c_T\, d_{1,1} & -c_T\, d_{1,2} & \dots & -c_T\, d_{1,N} \\ \lambda_1\, c_Q & \lambda_2\, c_Q & \dots & \lambda_N\, c_Q \end{bmatrix} \begin{bmatrix} \varpi_1^2 \\ \varpi_2^2 \\ \vdots \\ \varpi_N^2 \end{bmatrix} \tag{9}$$

If $N = 4$ one can determine the desired angular rates of the rotors by inverting (9). When the UAV is actuated by more than four rotors, the set of equations (9) is overdetermined and the Moore-Penrose pseudo-inverse method can be used to determine the desired angular velocities of the propellers. Besides, improvements for the Moore-Penrose pseudo-inverse are reported in recent studies [2], [16].

System (8) shows full actuation of the rotational dynamics and underactuation of the translational dynamics. For the rotational motion, exponential convergence of the angular velocity $\boldsymbol{\omega}$ to any bounded desired value $\boldsymbol{\omega}_d$ is easy to obtain, since the subsystem Σ_2 is fully actuated and the angular velocity vector $\boldsymbol{\omega}$ can be measured at high frequency by an onboard gyroscope. A possible control solution is [15]

$$\boldsymbol{\Gamma} = -K_\omega(\boldsymbol{\omega} - \boldsymbol{\omega}_d) + \boldsymbol{\omega}_d \times \mathbf{J}\boldsymbol{\omega} + \mathbf{J}\dot{\boldsymbol{\omega}}_d, \tag{10}$$

with a diagonal positive gain matrix K_ω. The disturbance torque $\boldsymbol{\Gamma}_e$, caused mainly by parasitic, flapping and induced drag forces, is counteracted by a sufficiently large gain K_ω. From here on, all attention of the control design can be given to the control of the subsystem Σ_1 using T and $\boldsymbol{\omega} \equiv \boldsymbol{\omega}_d$ as control inputs.

III. Hierarchical Nonlinear Control Architecture

Figure 4 shows the proposed cascaded control structure for several control modes associated with different levels of motion autonomy. The hierarchical control approach adopted here is inspired by the two control approaches proposed in [8] and [12]. A "low-level" fast inner-loop stabilizes the vehicle's thrust direction (i.e. thrust magnitude + thrust orientation) and a "high-level" slow outer-loop controls the translational dynamics. This control strategy is based on the principles of: (i) using the thrust magnitude and the vehicle's thrust orientation as intermediary control variables to control the translational dynamics, and (ii) applying a high-gain controller to stabilize the desired thrust direction using the angular velocity as control input.

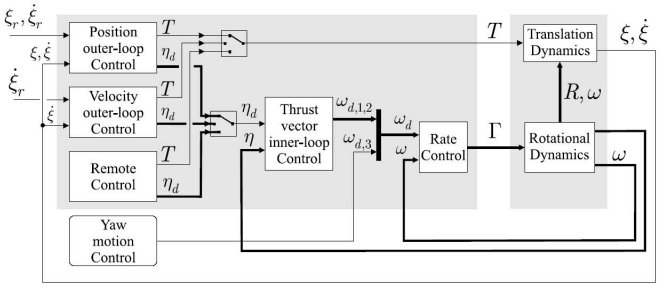

Fig. 4. Hierarchical nonlinear control architecture.

A. Inner-loop Thrust-direction Control

The objective is to stabilize the thrust orientation $\boldsymbol{\eta} := \mathbf{R}\mathbf{e}_3 \in \mathbb{S}^2$ to a given desired unit vector $\boldsymbol{\eta}_d \in \mathbb{S}^2$ which can be specified either by a remote control or by the intermediary control of the outer-loop (see Fig. 4). This objective is achieved by computing the first and second components of the desired angular velocity $\boldsymbol{\omega}_{d,1,2} := (\omega_{d,1}, \omega_{d,2})^\top$ as follows [8]:

$$\boldsymbol{\omega}_{d,1,2} = \left(\mathbf{R}^\top \left(k_\eta \frac{\boldsymbol{\eta} \times \boldsymbol{\eta}_d}{(1+\boldsymbol{\eta}^\top \boldsymbol{\eta}_d)^2} - (\boldsymbol{\eta}_\times)^2 (\boldsymbol{\eta}_d \times \dot{\boldsymbol{\eta}}_d) \right) \right)_{1,2} \tag{11}$$

with a positive gain k_η. Exponential stability of the equilibrium $\boldsymbol{\eta} = \boldsymbol{\eta}_d$ is ensured, provided that $\boldsymbol{\eta}(0) \neq -\boldsymbol{\eta}_d(0)$ (see [8] for the proof). The control law (11) indicates that only the first two components of $\boldsymbol{\omega}_d$, i.e. $\boldsymbol{\omega}_{d,1,2}$, are involved in the realization of the thrust orientation control objective. Thus, the remaining component of $\boldsymbol{\omega}_d$, i.e. $\omega_{d,3}$, can be used for a complementary objective related to the yaw motion.

B. Outer-loop Position Control

The objective consists in stabilizing the vehicle's position $\boldsymbol{\xi}$ to a reference trajectory defined by $\boldsymbol{\xi}_r \in \mathbb{R}^3$ by using the thrust intensity T and the thrust orientation $\boldsymbol{\eta} \equiv \boldsymbol{\eta}_d$ as control inputs. Denote $\tilde{\boldsymbol{\xi}} := \boldsymbol{\xi} - \boldsymbol{\xi}_r$ the trajectory tracking error and $\dot{\tilde{\boldsymbol{\xi}}} := \dot{\boldsymbol{\xi}} - \dot{\boldsymbol{\xi}}_r$ the velocity error.

Using (8a) one obtains the following translational error dynamics:

$$\ddot{\tilde{\boldsymbol{\xi}}} = -\frac{1}{m} T \boldsymbol{\eta} + \boldsymbol{\gamma}_e - \ddot{\boldsymbol{\xi}}_r, \tag{12}$$

with the external acceleration $\boldsymbol{\gamma}_e := \mathbf{F}_e/m$. Eq. (12) can be rewritten as

$$\begin{cases} \ddot{\tilde{\boldsymbol{\xi}}} &= -h(\tilde{\boldsymbol{\xi}}, \dot{\tilde{\boldsymbol{\xi}}}) - \frac{1}{m} T \boldsymbol{\eta} + \boldsymbol{\gamma} \\ \boldsymbol{\gamma} &:= h(\tilde{\boldsymbol{\xi}}, \dot{\tilde{\boldsymbol{\xi}}}) + \boldsymbol{\gamma}_e - \ddot{\boldsymbol{\xi}}_r \end{cases} \tag{13}$$

with $h_. : \mathbb{R}^3 \to \mathbb{R}^3$ a bounded function chosen in order to make $\tilde{\boldsymbol{\xi}} = 0$ a globally asymptotically stable equilibrium of the equation $\ddot{\tilde{\boldsymbol{\xi}}} = -h(\tilde{\boldsymbol{\xi}}, \dot{\tilde{\boldsymbol{\xi}}})$. We now have to ensure the asymptotic stability of $m\boldsymbol{\gamma} - T\boldsymbol{\eta} = 0$. To this end, assuming that $\boldsymbol{\gamma}$ does not vanish, we propose the following outer-loop control:

$$(T, \boldsymbol{\eta}_d) = (m|\boldsymbol{\gamma}|, \boldsymbol{\gamma}/|\boldsymbol{\gamma}|) \tag{14}$$

and apply the inner-loop control $\boldsymbol{\omega}_{d,1,2}$ defined by (11).

In traditional literature on control of small-scale UAVs, gravity is considered to be the only external force acting on the system. In this case, the computation of the desired acceleration $\boldsymbol{\gamma}$ is straight-forward. If the flapping and induced drag forces are included, the computation of $\boldsymbol{\gamma}$ becomes more involved. This is due to the fact that the drag forces are a function of the orientation $\mathbf{R}$ of the UAV. With the inclusion of the drag forces in the controller, the desired acceleration, which determines the desired orientation of the UAV, is now a function of the orientation itself. As a consequence, a closed form solution for the desired acceleration may not exist (see [8], [7] for more discussions on this issue). In section III-C, we discuss a novel solution to this issue. For now, we assume that we approximately know the external acceleration $\boldsymbol{\gamma}_e$ and that it is independent of both the thrust magnitude T and the rotation $\mathbf{R}$.

Note that the desired thrust orientation $\boldsymbol{\eta}_d$ given in (14) is not well-defined if the term $\boldsymbol{\gamma}$ vanishes (see [8], [7] for more discussions on this issue). In order to limit the risk of a vanishing $\boldsymbol{\gamma}$, a function $h(\tilde{\boldsymbol{\xi}}, \dot{\tilde{\boldsymbol{\xi}}})$ is chosen to be uniformly smaller in norm than the gravity constant g (corresponding to the norm of $\boldsymbol{\gamma}_e$ when hovering in the absence of wind). We propose to consider:

$$h(\tilde{\boldsymbol{\xi}}, \dot{\tilde{\boldsymbol{\xi}}}) = \begin{bmatrix} \mathrm{sat}_{\Delta_1^p}(k_1^p \tilde{\boldsymbol{\xi}}_{1,2}) + \mathrm{sat}_{\Delta_1^v}(k_1^v \dot{\tilde{\boldsymbol{\xi}}}_{1,2}) \\ \mathrm{sat}_{\Delta_3^p}(k_3^p \tilde{\xi}_3) + \mathrm{sat}_{\Delta_3^v}(k_3^v \dot{\tilde{\xi}}_3) \end{bmatrix}, \tag{15}$$

with the classical saturation function $\mathrm{sat}_\Delta(\mathbf{x}) := \mathbf{x} \min(1, \Delta/|\mathbf{x}|)\ \forall \mathbf{x} \in \mathbb{R}^n$, and with k_1^p, k_1^v, k_3^p, k_3^v, Δ_1^p, Δ_1^v, Δ_3^p, Δ_3^v some positive numbers, ensures the almost global asymptotic stability of the equilibrium $(\tilde{\boldsymbol{\xi}}, \dot{\tilde{\boldsymbol{\xi}}}) = (0, 0)$ of the nominal system $\ddot{\tilde{\boldsymbol{\xi}}} = -h(\tilde{\boldsymbol{\xi}}, \dot{\tilde{\boldsymbol{\xi}}})$. Thus, the use of $h(\tilde{\boldsymbol{\xi}}, \dot{\tilde{\boldsymbol{\xi}}})$ in the definition of $\boldsymbol{\gamma}$ in (13), together with the outer-loop control (14) of $(T, \boldsymbol{\eta}_d)$ and the inner-loop control (11) of $\boldsymbol{\omega}_{d,1,2}$, ensures the almost-global stability of the equilibrium $(\tilde{\boldsymbol{\xi}}, \dot{\tilde{\boldsymbol{\xi}}}, \boldsymbol{\eta}) = (0, 0, \boldsymbol{\eta}_d)$, provided that $\boldsymbol{\gamma}$ never crosses zero. Note that the saturation functions in the definition (15) of $h(\tilde{\boldsymbol{\xi}}, \dot{\tilde{\boldsymbol{\xi}}})$ are introduced in order to reduce the risk of a vanishing $\boldsymbol{\gamma}$. Additionally, this allows for the local decoupling of the vehicle's horizontal and vertical dynamics in closed loop.

To further add robustness with respect to the imprecise knowledge of $\boldsymbol{\gamma}_e$ and other unmodeled dynamics, an integral term should be incorporated into the control law. To this end and also to limit the integral wind-up effects largely discussed in the literature (e.g. [8], [17]), the following bounded integrator is introduced (similar to the one proposed in [8]):

$$\begin{aligned} \ddot{\mathbf{z}}_{1,2} &= -2k_1^z \dot{\mathbf{z}}_{1,2} - (k_1^z)^2 (\mathbf{z}_{1,2} - \mathrm{sat}_{\Delta_1^z}(\mathbf{z}_{1,2})) + \mathrm{sat}_{\Delta_1^{pz}}(k_1^{pz} \tilde{\boldsymbol{\xi}}_{1,2}) \\ \ddot{z}_3 &= -2k_3^z \dot{z}_3 - (k_3^z)^2 (z_3 - \mathrm{sat}_{\Delta_3^z}(z_3)) + \mathrm{sat}_{\Delta_3^{pz}}(k_3^{pz} \tilde{\xi}_3) \\ \mathbf{z}(0) &= 0, \quad \dot{\mathbf{z}}(0) = 0, \end{aligned} \tag{16}$$

with $k_1^z, k_1^{pz}, k_3^z, k_3^{pz}, \Delta_1^z, \Delta_1^{pz}, \Delta_3^z, \Delta_3^{pz}$ some positive numbers. Defining new tracking error variables $\tilde{\boldsymbol{\xi}}_z := \tilde{\boldsymbol{\xi}} + \mathbf{z}$ and $\dot{\tilde{\boldsymbol{\xi}}}_z := \dot{\tilde{\boldsymbol{\xi}}} + \dot{\mathbf{z}}$ and using (12) one deduces

$$\begin{cases} \ddot{\tilde{\boldsymbol{\xi}}}_z &= -h(\tilde{\boldsymbol{\xi}}_z, \dot{\tilde{\boldsymbol{\xi}}}_z) - \frac{1}{m} T \boldsymbol{\eta} + \boldsymbol{\gamma}_z^p \\ \boldsymbol{\gamma}_z &:= h(\tilde{\boldsymbol{\xi}}_z, \dot{\tilde{\boldsymbol{\xi}}}_z) + \boldsymbol{\gamma}_e - \ddot{\boldsymbol{\xi}}_r + \ddot{\mathbf{z}} \end{cases} \tag{17}$$

with the function $h(\cdot)$ defined by (15) with $(\tilde{\boldsymbol{\xi}}, \dot{\tilde{\boldsymbol{\xi}}})$ replaced by $(\tilde{\boldsymbol{\xi}}_z, \dot{\tilde{\boldsymbol{\xi}}}_z)$. Now, similarly to the position controller described previously, one can define the outer-loop control (14) of

$(T, \boldsymbol{\eta}_d)$ with $\boldsymbol{\gamma}$ replaced by $\boldsymbol{\gamma}_z$ and apply the inner-loop control (11) of $\boldsymbol{\omega}_{d,1,2}$ in order to ensure the convergence of $\tilde{\boldsymbol{\xi}}_z$ to zero. From here, using the definition of $\tilde{\boldsymbol{\xi}}_z$ and the dynamics of $\mathbf{z}$ (16), it is not difficult to show the convergence of $\tilde{\boldsymbol{\xi}}$ to zero (see [8] for a similar proof).

C. Including Blade Flapping and Induced Drag

When drag forces due to blade flapping and induced drag are incorporated in the control design, one may include them in the external force as $\mathbf{F}_e = mg\mathbf{e}_3 - T\mathbf{R}\mathbf{A}_{drag}\mathbf{R}^\top\dot{\boldsymbol{\xi}}$. However, as explained in Sec. III-B, the desired acceleration, which determines the desired thrust orientation $\boldsymbol{\eta}_d = (\mathbf{R}\mathbf{e}_3)_d$ of the UAV, is now a function of the orientation. Therefore, a closed form solution for the desired acceleration may not exist. However, we can rewrite the drag forces as

$$\begin{aligned} T\mathbf{R}\mathbf{A}_{drag}\mathbf{R}^\top\dot{\boldsymbol{\xi}} &\approx T\mathbf{R}\begin{bmatrix} c_a+c_d & 0 & 0 \\ 0 & c_a+c_d & 0 \\ 0 & 0 & 0 \end{bmatrix}\mathbf{R}^\top\dot{\boldsymbol{\xi}} \\ &\approx T(c_a+c_d)\left(\mathbf{R}\mathbf{R}^\top - \mathbf{R}\mathbf{e}_3\mathbf{e}_3^\top\mathbf{R}^\top\right)\dot{\boldsymbol{\xi}} \\ &\approx T(c_a+c_d)\left(\dot{\boldsymbol{\xi}} - \mathbf{R}\mathbf{e}_3 v_3\right) \end{aligned}$$

where v_3 is the vehicles velocity in $\mathbf{e}_3$ direction in the body-fixed frame and assuming that the vehicle is symmetrical $c_{dx} = c_{dy} = c_d$. Additionally, we assume that the coefficient c_b is very small compared to $c_a + c_d$ and therefore negligible.

Revisiting the translational dynamics model Eq. (8a), we can now include the drag forces as

$$\begin{aligned} m\ddot{\boldsymbol{\xi}} &= -T\mathbf{R}\mathbf{e}_3 + \mathbf{F}_e \\ &= -T\mathbf{R}\mathbf{e}_3 + mg\mathbf{e}_3 - T(c_a+c_d)\left(\dot{\boldsymbol{\xi}} - \mathbf{R}\mathbf{e}_3 v_3\right) \\ &= -T(1-(c_a+c_d)v_3)\mathbf{R}\mathbf{e}_3 - T(c_a+c_d)\dot{\boldsymbol{\xi}} + mg\mathbf{e}_3 \end{aligned} \tag{18}$$

Furthermore, the additive drag term can be rewritten as

$$T(c_a+c_d)\dot{\boldsymbol{\xi}} = (mg+\delta)(c_a+c_d)\dot{\boldsymbol{\xi}} \approx mg(c_a+c_d)\dot{\boldsymbol{\xi}} \tag{19}$$

assuming that the offset δ between the magnitude of the actual thrust and the hovering thrust is small and is compensated by the integral term in the controller when the UAV is moving at constant velocity. In case of a varying velocity, the tracking error is compensated by a sufficiently large gain of the D-part of the controller.

By inspection of Eq. (18), we can now compute the augmented thrust vector magnitude $\bar{T}$ that compensates for the drag by

$$\bar{T} = T\left(1 - (c_a+c_d)v_3\right) \tag{20}$$

Equivalently, the external acceleration $\boldsymbol{\gamma}_e$ is now

$$\boldsymbol{\gamma}_e = g\mathbf{e}_3 - g(c_a+c_d)\dot{\boldsymbol{\xi}}. \tag{21}$$

The drag-compensated external acceleration can now be incorporated in the position controller Eq. (17). The magnitude of the thrust vector is then computed using Eq. (14) and subsequently drag compensated using Eq. (20).

IV. Results

A. UAV Platform

The presented control scheme is implemented and evaluated on the Flybox hexacopter UAV designed and built by Skybotix AG. The UAV is depicted in Fig. 5. The mechanical, electrical and software setup of the platform are described in detail in [5], the general description of the control setup, as used for these experiments is found in [3]. Table I depicts the specifications of the Flybox UAV that are also used in simulation.

Fig. 5. Flybox UAV in the hexacopter configuration.

TABLE I
Specifications of Flybox UAV

Specification	Numerical Value
Mass m [kg]	1.9
Moment of Inertia $\mathbf{J}$ [kg m^2]	diag(0.031,0.061, 0.085)
Time constant motor τ [s]	0.09
First order drag $g(c_a + c_d)[s^{-1}]$	0.21
Second order drag c_{aero} [-]	0.15

B. Identification Drag Coefficient

In order to compensate for the blade flapping and induced drag in the control scheme, we first identify the lumped drag coefficient $(c_a + c_d)$ in a batch-estimation offline scheme.

We can show that the accelerometer output and the vehicle's velocity can be directly related to the drag coefficient. The accelerometer output $\mathbf{a}_m \in \mathbb{R}^3$ is composed of the gravity vector $g\,\mathbf{e}_3$, the linear acceleration $\ddot{\boldsymbol{\xi}}$ in the inertial frame as well as a slowly time-varying accelerometer bias $\mathbf{b}_a \in \mathbb{R}^3$ and measurement noise $\mathbf{n}_a$ in the body-fixed frame and can be expressed as

$$\mathbf{a}_m = \mathbf{R}^\top(\ddot{\boldsymbol{\xi}} - g\,\mathbf{e}_3) - \mathbf{b}_a - \mathbf{n}_a \tag{22}$$

Combining this accelerometer model with the translational UAV model (18), which includes the drag dynamics, one can write

$$\begin{aligned} \mathbf{a}_m &= \mathbf{R}^\top\left(-\tfrac{T}{m}\mathbf{R}\mathbf{e}_3 - \tfrac{T}{m}(c_a+c_d)(\dot{\boldsymbol{\xi}} - \mathbf{R}\mathbf{e}_3 v_3)\right) - \mathbf{b}_a - \mathbf{n}_a \\ \mathbf{a}_m &= -\tfrac{T}{m}\begin{bmatrix}(c_a+c_d)v_1 \\ (c_a+c_d)v_2 \\ 1\end{bmatrix} - \mathbf{b}_a - \mathbf{n}_a \end{aligned} \tag{23}$$

where v_1 and v_2 are the velocities in direction $\mathbf{e}_1$ and $\mathbf{e}_2$ in the body-fixed frame.

If the thrust magnitude T is not known, the UAV's altitude can be set to a constant value during the system identification flight and it can be assumed that the thrust T is approximately mg. This assumption is justifiable as long as the UAV is close to hovering, e.g. the roll and pitch angles

are small and the horizontal velocities do not exceed $1m/s$. The latter requirement is also justifiable by the fact that at velocities larger $1m/s$, the second order body-drag becomes apparent.

To identify the lumped drag parameter, we perform a UAV flight in a motion tracking system which provides high-precision pose information at 200 Hz. The pose is fused with the onboard IMU in an EKF [4][1] to obtain an estimate of the accelerometer bias and body velocity.

By inspection of Eq. (23), the lumped drag parameter can be identified using linear least squares:

$$(c_a + c_d) = -g \begin{bmatrix} (\mathbf{a}_m + \mathbf{b}_a)_{,1}^\top \mathbf{e}_1 \\ (\mathbf{a}_m + \mathbf{b}_a)_{,1}^\top \mathbf{e}_2 \\ \vdots \\ (\mathbf{a}_m + \mathbf{b}_a)_{,N}^\top \mathbf{e}_1 \\ (\mathbf{a}_m + \mathbf{b}_a)_{,N}^\top \mathbf{e}_2 \end{bmatrix}^\dagger \begin{bmatrix} \mathbf{v}_{,1}^\top \mathbf{e}_1 \\ \mathbf{v}_{,1}^\top \mathbf{e}_2 \\ \vdots \\ \mathbf{v}_{,N}^\top \mathbf{e}_1 \\ \mathbf{v}_{,N}^\top \mathbf{e}_2 \end{bmatrix} \tag{24}$$

where $(\mathbf{a}_m - \mathbf{b}_a)_{,i}$ and $\mathbf{v}_{,i}$ denote the bias corrected accelerometer and body velocity measurement at timestep i during the identification flight.

In Fig. 6, the estimation of the drag parameter for the Flybox UAV is visualized. The lumped drag coefficient $g(c_a + c_d)$ corresponds to the slope of the fitted line. In the lower plot, the velocity estimated from the Vicon system is compared to the velocity that is predicted using the accelerometer output and the drag model Eq. (23).

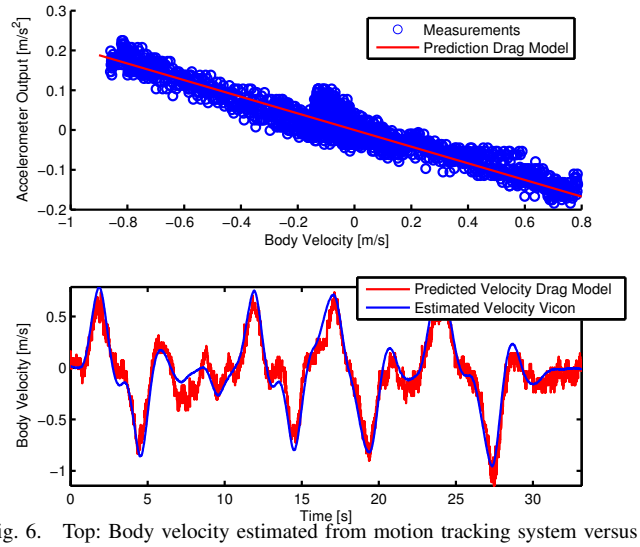

Fig. 6. Top: Body velocity estimated from motion tracking system versus bias corrected accelerometer output. Slope of fitted line corresponds to $g(c_a + c_d)$ drag parameter. Bottom: Body velocity (blue) and predicted body velocity from accelerometer output using drag model (red).

C. Simulation Results

First, the proposed control scheme is evaluated in a set of simulations. The dynamics of the simulated UAV flight are governed by Eqs. (1) and (2). The motors are modeled as a linear first-order system. Additionally, a second-order aerodynamic drag force is included and is modeled as $\mathbf{F}_{aero} = -c_{aero}|\dot{\boldsymbol{\xi}}|\dot{\boldsymbol{\xi}}$. The drag coefficient c_{aero} is considered to be constant and independent of the angle of attack of the relative airflow with respect to the UAV. The coefficients used in simulation reflect the values that have been identified for the vehicle used in the real experiments and are depicted in Tab. I.

1) Response to Position Reference Ramp: In a first experiment, the response of the controller to a ramp input in position reference is evaluated. The experiment starts with the UAV in hover. At $t = 1\,s$, the UAV starts moving with a reference velocity $|\dot{\boldsymbol{\xi}}_r| = 1\,m/s$ in $\mathbf{e}_1$ direction. At $t = 11\,s$, the UAV position setpoint is set to hover again.

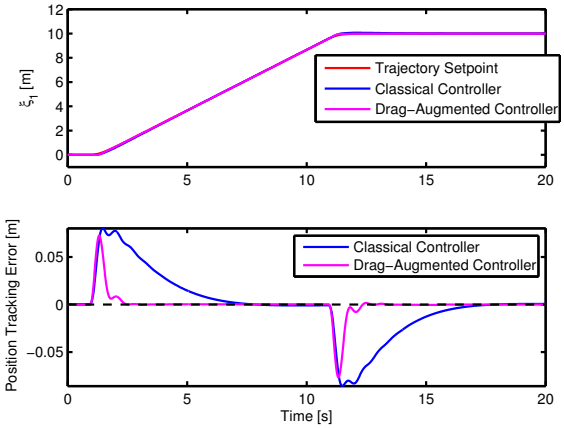

Fig. 7. Response of classical- and drag augmented controller to a ramp input with a velocity setpoint of 1 m/s.

If the flapping compensation is disabled, the UAV is a bit "behind" the setpoint, as depicted in Fig. 7. Using the integral control term, the UAV will eventually approach the moving position setpoint with the integral term counteracting the approximately constant drag force. When the setpoint comes to a stop at $t = 11\,s$, there is a significant overshoot due to the integrator which is still compensating for the (now non-existing) drag force. With the flapping compensation enabled, the UAV realized (almost) perfectly the tracking control objective.

The experiment is repeated using a larger velocity setpoint $|\dot{\boldsymbol{\xi}}_r| = 3\,m/s$ in $\mathbf{e}_1$ direction, as depicted in Fig. 8. While the drag-compensated controller still outperforms the classical controller, the drag-compensated controller now shows imperfect trajectory tracking. This is due to two effects. Firstly, the second order drag effects become significant at such speeds and act as a disturbance on the trajectory tracking. Secondly, the assumption made in Eq. (19), that the thrust is approximately mg at hovering, is violated. At such speeds, the required thrust is around 20% higher than the hovering thrust only due to the flapping and induced drag. This difference as well as the influence of the second order drag has to be compensated again by the integrator and can be clearly seen in the time response of the controller. By assuming that the second order drag is independent of the orientation of the UAV, this force could be included in the controller by extending the external acceleration to $\boldsymbol{\gamma}_e = g\mathbf{e}_3 - g(c_a + c_d)\dot{\boldsymbol{\xi}} - \frac{c_{aero}}{m}|\dot{\boldsymbol{\xi}}|\dot{\boldsymbol{\xi}}$.

[1]It has to be noted that a motion tracking system is not necessary for system identification since this EKF is able to estimate $\mathbf{v}$ and $\mathbf{b}_a$ using a low-cost position sensor (e.g. GPS sensor) only.

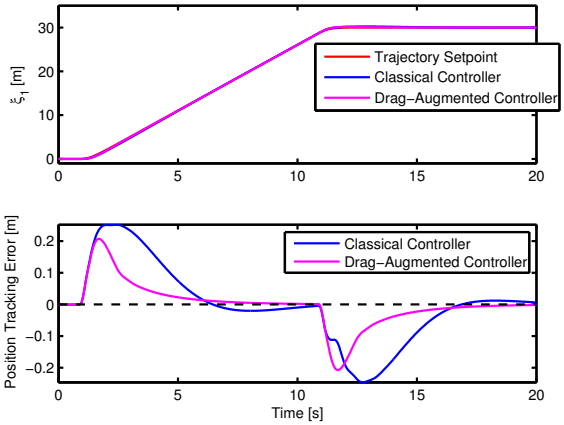

Fig. 8. Response of classical- and drag augmented controller to a ramp input with a velocity setpoint of 3 m/s.

D. Experiments

The performance of the proposed hierarchical position control scheme is evaluated on the hexacopter platform Flybox indoors in a Vicon motion tracking system. The full pose of the UAV and its velocity is estimated on-board the UAV by fusing position and attitude from the Vicon with the accelerometer and gyrocope output from the IMU in an EKF [4]. Due to space limitations of the motion tracking room, the control scheme is evaluated via a step input in position. In Fig. 9, the step response of the controller with and without the drag augmentation is depicted. The initial control error on

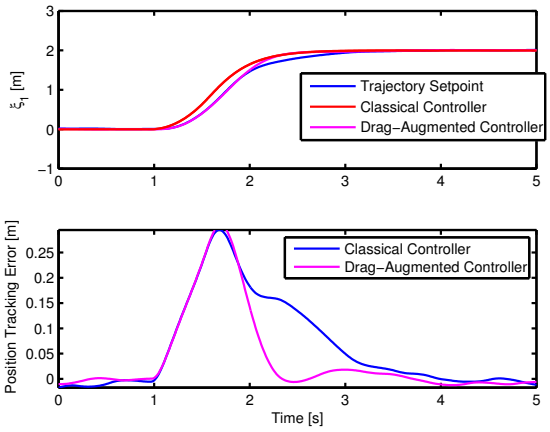

Fig. 9. Response of the Flybox UAV to a step input of 2 m using classical- and drag-augmented controller. Maximal reference velocity and acceleration of step trajectory is 2.5 m/s and 4 m/s^2 respectively.

both controllers can be attributed to the low-pass behaviour of the motors and the inertia of the UAV[2]. Once the UAV picks up speed, the drag-augmented controller outperforms the traditional controller due to the drag compensation and converges faster to the setpoint.

V. Conclusions

In this paper, the design and evaluation of a novel nonlinear flight control system for multirotor UAVs is presented and evaluated. We show that the control performance of the UAV during trajectory tracking is affected significantly by drag forces due to blade flapping and induced drag. The presented cascaded nonlinear control scheme takes into account the nonlinear nature of these aerodynamic drag forces while being respectful of the UAV's motion in 3D-space thus allowing for a large domain of operation. We show in both simulation and in real experiments that the drag-augmented control scheme improves trajectory tracking performance and reduces the need for integral control action.

[2]The Flybox UAV used in the experiment is traditionally used for industrial inspection and has an moment of inertia which is a magnitude larger than the inertia of the AscTec Hummingbird, usually used in such experiments[11].

Acknowledgment

The authors acknowledge the financial support by the ECHORD TUAV project, the FP7 ICARUS project (285417) and by the Robotex ANR fund. The authors would like to thank Skybotix AG for their support.

References

[1] P.-J. Bristeau, F. Callou, D. Vissière, and N. Petit. The Navigation and Control technology inside the AR.Drone micro UAV. In *IFAC World Congress*, pages 1477–1484, 2011.

[2] G. Ducard and M.-D. Hua. Discussion and practical aspects on control allocation for a multi-rotor helicopter. In *Conference on Unmanned Aerial Vehicle in Geomatics*, pages 1–6, 2011.

[3] S. Omari, G. Ducard, M.-D. Hua and T. Hamel. Bilateral Haptic Teleoperation of VTOL UAVs. *IEEE Conference on Robotics and Automation*, 2013.

[4] S. Weiss, M. Achtelik, M. Chli, R. Siegwart, Versatile Distributed Pose Estimation and Sensor Self-Calibration for an Autonomous MAV. In *IEEE Conference on Robotics and Automation*, pages 31–38, 2012.

[5] S. Omari, M.-D. Hua, G. Ducard and T. Hamel. Bilateral Haptic Teleoperation of an Industrial Multirotor UAV. *Springer Tracts of Advanced Robotics (STAR), Technology transfer experiments from the ECHORD project*, 2013.

[6] T. Hamel, R. Mahony, R. Lozano, and J. Ostrowski. Dynamic modelling and configuration stabilization for an X4-flyer. In *IFAC World Congress*, pages 200–212, 2002.

[7] M.-D. Hua, T. Hamel, P. Morin, and C. Samson. Introduction to Feedback Control of Underactuated VTOL Vehicles. *IEEE Control Systems Magazine*, 33(1):61–75, 2013

[8] M.-D. Hua, T. Hamel, P. Morin, and C. Samson. A control approach for thrust-propelled underactuated vehicles and its application to VTOL drones. *IEEE Transactions on Automatic Control*, 54(8):1837–1853, 2009.

[9] R. Mahony, V. Kumar, and P. Corke. Multirotor Aerial Vehicles: Modeling, Estimation, and Control of Quadrotor. *IEEE Robotics & Automation Magazine*, pages 20–32, 2012.

[10] P. Martin and E. Salaun. The true role of accelerometer feedback in quadrotor control. In *IEEE Conference on Robotics and Automation*, pages 1623–1629, 2010.

[11] D. Mellinger, Q. Lindsey, M. Shomin and V Kumar. Design, modeling, estimation and control for aerial grasping and manipulation. *IEEE Conference on Intelligent Robots and Systems* , pages 2668–2673, 2011.

[12] J.-M. Pflimlin, T. Hamel, P. Souères, and R. Mahony. A hierarchical control strategy for the autonomous navigation of a ducted fan flying robot. In *IEEE Conference on Robotics and Automation*, pages 2491–2496, 2006.

[13] P. Pounds, R. Mahony, and P. Corke. Modelling and control of a large quadrotor robot. *Control Engineering Practice*, 18(7):691–699, 2010.

[14] R. W. Prouty. *Helicopter Performance, Stability, and Control*. Krieger, 2002.

[15] K. Rudin, M.-D. Hua, G. Ducard, and S. Bouabdallah. A robust attitude controller and its application to quadrotor helicopters. In *IFAC World Congress*, pages 10379–10384, 2011.

[16] T. Schneider and G. Ducard. Fault-tolerant control allocation for multirotor helicopters using parametric programming. In *International Micro Air Vehicle Conference*, 2012.

[17] M.-D. Hua and C. Samson. Time sub-optimal nonlinear PI and PID controllers applied to longitudinal headway car control. *International Journal of Control*, 84(10):1717–1728, 2011.